ROYAL SOCIETY
OF CHEMISTRY

PAPER

Check for updates

Hole-transport layer-dependent degradation mechanisms in perovskite solar modules

Marco Casareto, [ab] Saivineeth Penukula, [b] Wanyi Nie[c] and Nicholas Rolston ⋆[b]

It is imperative to understand how the design of perovskite solar modules (PSMs) affects their degradation mechanisms and byproducts under environmental stressors to enable their long-term reliability. This work reports on the impact of the hole-transport layer (HTL) on thermal cyclability and degradation mechanisms of p–i–n PSMs by comparing 3 HTLs: NiO_x, MeO-2PACz (a self-assembled monolayer), and a bilayer HTL of MeO-2PACz on NiO_x. We observe surprising thermal cyclability from a performance standpoint despite generating clear degradation products. We find that without a fully dense HTL, seemingly insignificant moisture/oxygen ingress through the edge of the PSMs can lead to rapid destabilization of the metal halide perovskite (MHP) layer due to reactions between MHP degradation byproducts and the indium-tin oxide layer. We also show that illumination-induced cation phase segregation is dependent on the illumination of an inactive area (regions of the substrate uncovered by the rear electrode). As such, we find that a dense interface between the MHP and ITO is necessary for chemically robust PSMs and highlight criteria for testing field-relevant configurations in lab-scale architectures.

Broader context

Environmental stressors such as thermal cycling, light, and moisture can cause significant degradation in perovskite solar modules (PSMs), hindering their advancement for commercial viability. There is a need to better identify and understand differences in material-specific degradation byproducts for state-of-the-art hole-transport layers (HTLs). This work compares the performance of encapsulated PSMs utilizing three different HTLs: a self-assembled monolayer (MeO-2PACz), a metal oxide (NiO_x), and a bilayer consisting of MeO-2PACz deposited on top of NiO_x. The differences in degradation byproducts and mechanisms unveil the importance of material selection with the end goal of commercial viability and long-term stability.

Introduction

Perovskite solar cells (PSCs) have made significant advances in recent years in their efficiency and stability, having reached 27% power conversion efficiency (PCE) from advancements in the metal halide perovskite (MHP) absorber layer, hole transport layers (HTLs), interlayers, and encapsulation techniques.[1–3] However, field-related issues with stability persist due to both intrinsic (ion migration, phase segregation, thermal instability) and extrinsic (moisture, oxygen) factors, the latter of which can primarily be addressed through improved packaging.[2–6] These issues are more apparent in perovskite solar modules (PSMs) that introduce new interfaces through selective laser scribing of layers within the device stack to allow for a series connection of adjacent cells.[7] The addition of laser scribing, along with challenges in maintaining the same quality of absorber and charge

transport layers for larger active areas, can lead to accelerated degradation of PSMs not seen with laboratory-scale PSCs.

Self-assembled monolayer (SAM)-based HTLs are increasingly used individually or as a passivating layer on commonly-used HTLs, such as NiO_x, in the p–i–n architecture as a "bilayer" configuration.[8–10] The synthesis of SAMs can be quite complex as they can be comprised of various organic groups for each part of the SAM, and the most commonly used SAMs (referred to as carbazole-based) are comprised of a phosphonic acid, alkyl chain, and carbazole group for the anchor, spacer, and terminal (functional) groups, respectively.[9,11] The use of SAMs as a standalone HTL has enabled consistent achievement of PCEs over 20% with the p–i–n architecture.[9,12] The bilayer configurations of HTLs have become increasingly popular as they allow for enhancement of a robust and reliable interface through passivation of dangling bonds, enhancement of the thermal stability of SAM-based devices, improvement in reverse-bias stability, and may aid in the suppression of harmful redox reactions, such as those between the MHP layer and high-valence Ni^{3+} and Ni^{4+} ions found on the surface of NiO_x.[12–15]

There have been several innovative implementations of SAMs to aid in their reproducibility and scalability through improved coverage, such as by using mixed SAMs, in which two

[a]Materials Science and Engineering, Fulton Schools of Engineering, Arizona State University, Tempe, AZ 85287, USA

[b]Renewable Energy Materials and Devices Lab, School of Electrical, Computer, and Energy Engineering (ECEE), Arizona State University, Tempe, AZ 85281, USA. E-mail: nicholas.rolston@asu.edu

[c]SUNY University at Buffalo, Department of Physics, Buffalo, NY 14260, USA

or more SAM molecules are used jointly, and co-deposition of the SAM with the MHP.[16–20] Changes in the chemical makeup and structure of SAMs have aided in addressing common degradation mechanisms seen in SAM-based devices, such as corrosion of underlying metal oxide layers or adverse reactions between the MHP and NiO_x/indium-tin oxide (ITO) layer.[21,22] Recent work found that MeO-2PACz (a commonly used SAM) improved the stability and performance of PSMs under damp heat testing when used in a bilayer configuration with NiO_x owing to the suppression of interfacial reactions between the MHP and NiO_x layers.[23] However, while there has been an increase in publications on the use of SAMs and/or SAM/NiO_x bilayers, there is still limited mechanistic understanding of the degradation mechanisms caused by different HTLs under environmental stressors. This work studies the differences in degradation mechanisms under stressors that include thermal cycling, moisture/oxygen ingress, and light exposure of PSMs with three different HTLs: NiO_x, MeO-2PACz, and a bilayer HTL of MeO-2PACz coated on top of NiO_x.

Results and discussion

Module fabrication for thermal cycling

This study utilizes a double-cation $Cs_{0.2}FA_{0.8}PbI_3$ MHP composition in a p–i–n device architecture: glass/ITO/HTL/MHP/C_{60}/BCP/Ag. We compare 3 different HTLs: a sol–gel NiO_x, MeO-2PACz, and a bilayer HTL consisting of MeO-2PACz deposited on top of NiO_x. A cross-section of the module architecture can be seen in Fig. 1(a), with the P1, P2, and P3 scribes labeled to allow for series interconnection between adjacent cells forming a 2-cell mini-module configuration. Fig. 1(b) shows a top-down schematic of a 25×25 mm ITO-patterned glass substrate with two 2-cell mini-modules. Regions on a PSM substrate covered by the rear electrode will be referred to as the "module" area, while

any MHP not covered by the rear electrode will be referred to as the "inactive" area. Initial PSM performance of the three HTLs after encapsulation can be seen in Fig. 1(c). As expected, the MeO-2PACz PSMs perform significantly better than NiO_x PSMs, primarily due to higher open-circuit voltages (V_{oc}) and fill factors (FF), as seen in Fig. S1 and shown in the literature.[24,25] However, while there are several MeO-2PACz PSMs that outperform bilayer PSMs, the median of the bilayer PSMs is slightly higher than the median of MeO-2PACz PSMs (14.6% vs. 14.1%), while their means are nearly identical, possibly indicating a lower variance and more reliable fabrication method for the bilayer architecture. This is likely due to improved coverage of MeO-2PACz on NiO_x vs. MeO-2PACz on ITO stemming from improved bonding of the phosphonic acid group to the substrate (tridentate vs. bidentate), as well as limiting the effect of any harmful shunts that may arise from the use of MeO-2PACz alone.[23,26] It is worth noting that while NiO_x as a standalone HTL offers lower performance than both other HTL configurations, it generally has a higher reproducibility than MeO-2PACz PSMs as MHP coverage on sol–gel NiO_x is seldom an issue. Additionally, single-cell devices had significant variability seen in MeO-2PACz PSCs with encapsulation, as seen in Fig. S2, due to V_{oc} and FF changes, potentially due to inhomogeneous contact at the MeO-2PACz/ITO and/or MHP/MeO-2PACz interfaces. Conversely, bilayer PSCs exhibited the most stable trend with encapsulation for all HTLs, indicating a uniform and dense HTL layer with improved interfacial contact with the MHP.

PSM stability for the different HTL configurations was first quantified through thermal cycling in an adapted manner of IEC 61215 from −40 to 85 °C at an accelerated rate of 4 °C min^{-1} with a dwell time of 10 minutes.[27] Fig. 2(a) shows PCE results for each HTL type after undergoing 300 thermal cycles with measurements at every 100 cycles. A dashed trendline follows
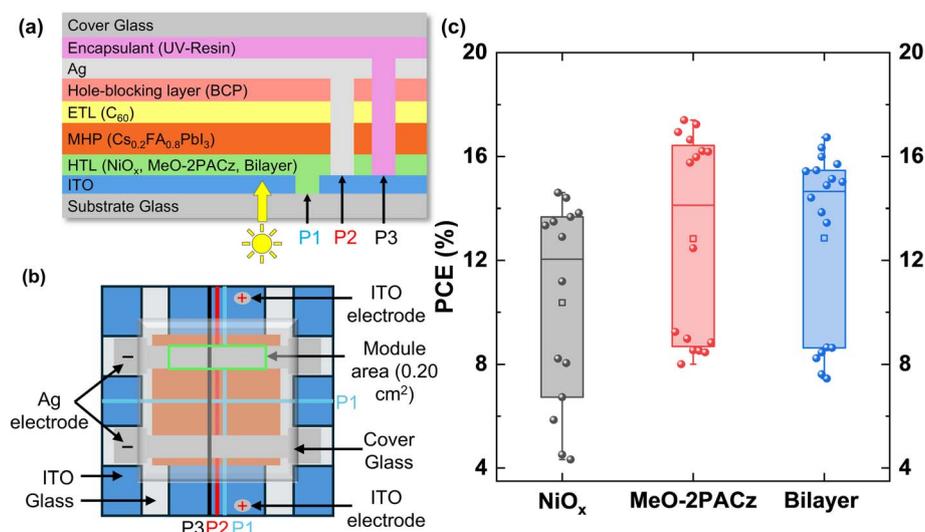

Fig. 1 (a) Schematic illustration of the PSM architecture, (b) top-down view of the PSM design on 25×25 mm ITO-patterned glass (area of a single PSM outlined in green), and (c) initial PSM power conversion efficiency (PCE) prior to thermal cycling (post-encapsulation). Box plots show each quartile (25th, 50th, and 75th percentiles), with whiskers representing the 5th and 95th percentiles and a square representing the mean.
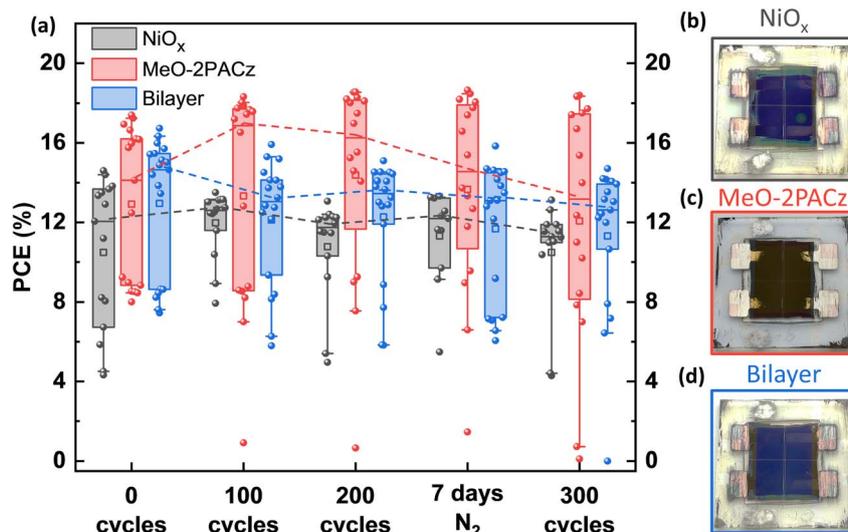
Fig. 2 (a) PSM power conversion efficiency (PCE) with thermal cycling for the three HTL architectures described. Dashed trend lines follow the progression of the box–plot median for each architecture. Photographs (taken from the ITO side) of representative (b) NiO$_x$, (c) MeO–2PACz, and (d) bilayer PSMs after 300 thermal cycles.

the median for each PSM configuration so as to limit the effect of outliers. NiO$_x$ PSMs were relatively stable throughout cycling while MeO-2PACz PSMs displayed a higher degree of variability, namely a ~20% relative increase in the median PCE after 100 cycles, which can be attributed to two PSMs nearly doubling their PCE from the "healing" of shunts, as their current–voltage behaviors show in Fig. S3. Notably, one of the PSMs in Fig. S3 reverted permanently to its shunted behavior after 200 cycles. We believe this variability in MeO-2PACz PSMs stems from less uniform coverage or poor interfacial contact at the MeO-2PACz/ITO and the MHP/MeO-2PACz interfaces, and the expansion and contraction of the MHP layer with thermal cycling may have remedied the contact between those layers. Bilayer PSMs displayed a drop in PCE after 100 cycles with a stabilization that lasted through 300 cycles. J_{sc}, V_{oc}, and FF trends with thermal cycling for each HTL can be seen in Fig. S4. All PSM configurations had noticeable drops in J_{sc} with thermal cycling which we will discuss when examining degradation byproducts. MeO-2PACz and bilayer PSMs maintain relatively stable V_{oc} and FF values throughout cycling.

Fig. 2(b)–(d) shows photographs of representative PSMs for each HTL architecture after 300 thermal cycles. Photographs were taken from the ITO (*i.e.*, sun-facing) side of the module stack to examine degradation in the module area under the Ag electrode. The visual degradation in MeO-2PACz PSMs seen in Fig. 2(c) appears as yellowing under the electrode originating from the edges of the module area. We also noticed a color change under the electrode of NiO$_x$ and bilayer PSMs after 300 cycles that appeared to be a lightening of the MHP layer, as seen in Fig. 2(b) and (d). It is worth noting that we observed no significant degradation originating from the scribe lines of the modules, regardless of the HTL configuration, contrary to previous reports.[6] Given this configuration and under these stressing conditions, reactions between the rear electrode and

MHP interface were not significant enough to lead to device failure.

Interestingly, we noticed a significant visual degradation accompanied by a drop in performance for MeO-2PACz PSMs that were kept in the dark in an N$_2$ glovebox for 7 days after 200 thermal cycles, as seen in the thermal cycling data in Fig. 2(a) and photographs in Fig. S5, primarily due to several MeO-2PACz PSMs losing about 10% of their relative J_{sc} values (Fig. S4). This delayed degradation was first observed with MeO-2PACz PSCs, wherein significant degradation occurred months after cycling and being stored in the dark in N$_2$, as seen in Fig. S6(a), accompanied by a slight drop in PCE for MeO-2PACz PSCs as shown in Fig. S6(b). A possible mechanism for the delayed degradation will be discussed in more detail later. The primary mode of degradation for MeO-2PACz PSCs is a reduction in the J_{sc}, as seen in Fig. S7, whereas NiO$_x$ PSCs remained relatively stable, even improving in PCE slightly.

Characterization of degradation products from thermal cycling

In order to identify the degradation byproducts, X-ray diffraction (XRD) was performed on post-mortem PSMs that were intentionally delaminated. Fig. 3(a)–(c) shows photographs of the delaminated PSMs after 300 thermal cycles, and solid rectangles show the module areas measured with XRD. Fig. 3(d) shows the XRD results of the module area of uncycled (lighter shade) and cycled (darker shade) PSMs for each HTL type. As seen in the XRD results in Fig. 3(d), the module area of thermally cycled MeO-2PACz PSMs displays peaks at $2\theta = 11.74°$ and $26.26°$, indicating the presence of δ-FAPbI$_3$ (hexagonal non-perovskite structure).[28,29] Additionally, Fig. 3(b) shows a lack of black MHP on the edges of the module area for cycled MeO-2PACz PSMs. These findings reveal that the degradation observed with thermal cycling for MeO-2PACz PSMs occurred
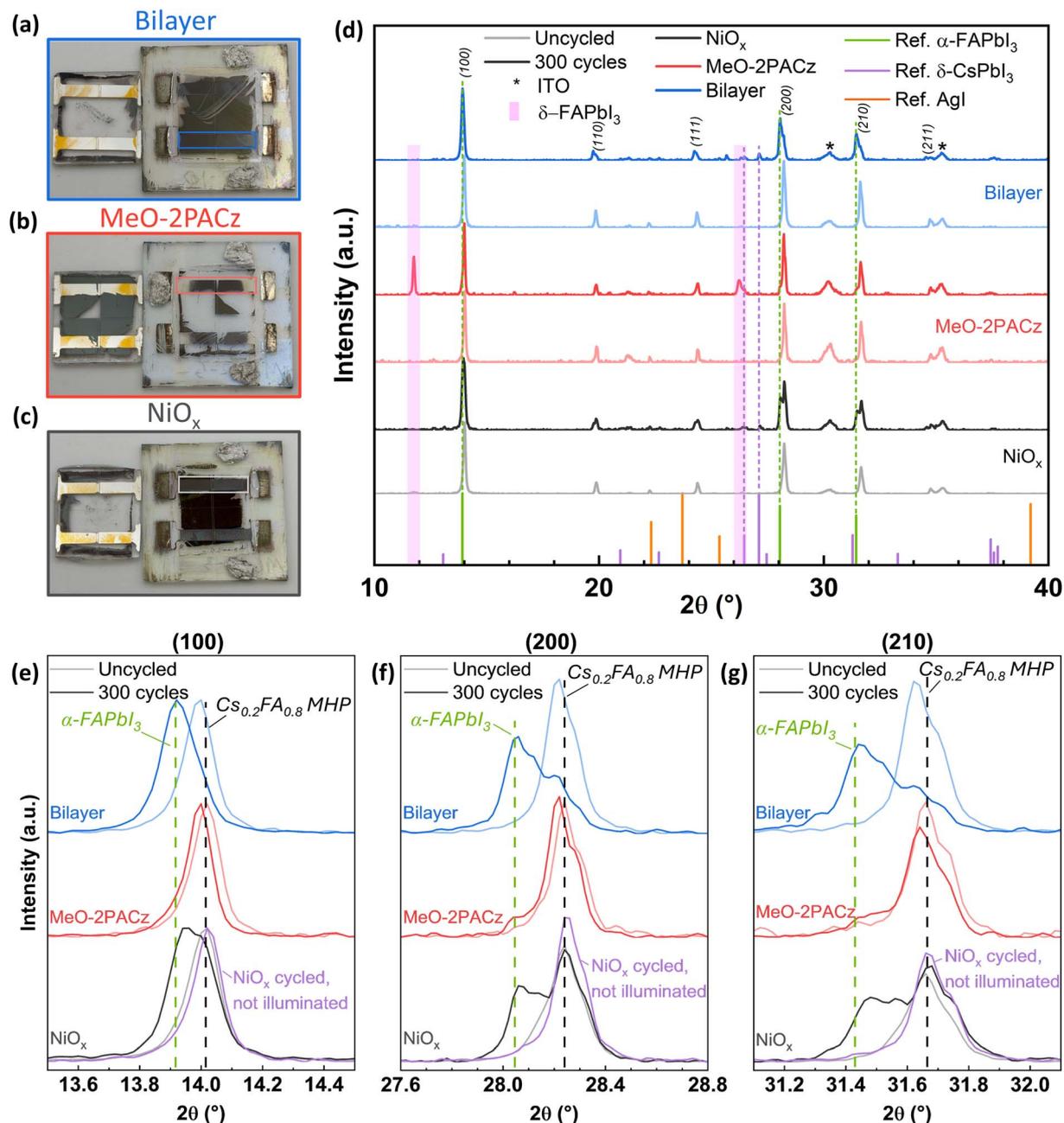
Fig. 3 Photographs of delaminated (a) bilayer, (b) MeO-2PACz, and (c) NiO$_x$ PSMs after 300 thermal cycles with solid rectangles outlining the module areas that were examined with X-ray diffraction (XRD). (d) XRD results of the module areas of uncycled and cycled PSMs, with reference patterns of α-FAPbI$_3$, δ-CsPbI$_3$, and AgI (ICDD ref. 00-069-0999, 04-016-2300, and 00-009-0374, respectively).[30–32] Only peaks with relative values greater than 0.2 of the maximum peak are shown for the reference patterns. (e)–(g) Magnified views of the XRD results from (d) for the (100), (200), and (210) planes with the addition of a cycled NiO$_x$ PSM that was never illuminated, highlighting the peak shifting in cycled NiO$_x$/bilayer PSMs. Dashed vertical lines represent reference scans for α-FAPbI$_3$ (green) and a pristine double-cation MHP (black).

from the MHP becoming more transparent as it transformed into δ-FAPbI$_3$, and the yellowing is primarily due to the reflection of C$_{60}$ on Ag. While no δ-FAPbI$_3$ was present in any of the NiO$_x$ PSMs and a relatively small number (2 out of 18) of bilayer PSMs displayed δ-FAPbI$_3$, 50% (10 out of 20) of cycled MeO-2PACz PSMs displayed δ-FAPbI$_3$ presence after 300 thermal cycles.

Cycled NiO$_x$/bilayer PSMs displayed peak shifting/splitting of the peaks corresponding to the (100), (200), and (210) planes (2θ = 14.02°, 28.24°, and 31.66°, respectively), as seen in Fig. 3(e)–(g), indicating the presence of α-FAPbI$_3$.[30–32] Additionally, cycled NiO$_x$/bilayer PSMs display peaks at 2θ = 26.46° and 27.11°, indicating the presence of δ-CsPbI$_3$ (yellow orthorhombic non-perovskite structure). These findings are suggestive of cation-phase segregation, a well-documented

phenomenon occurring with mixed cation MHPs that has been observed under illumination and heat.[33,34] Also shown in Fig. 3(e)–(g) is a NiO$_x$ PSM that was cycled but never illuminated/biased. Notably, this NiO$_x$ PSM does not display a peak shift after cycling, indicating the necessity for illumination to induce the observed cation phase segregation. We will comment on the significance of this finding later as we perform illumination-based testing. Meanwhile, the uncycled samples for all 3 HTLs had no noticeable degradation byproducts and demonstrated nearly identical XRD patterns with each other. The differences in degradation byproducts between MeO-2PACz and NiO$_x$/bilayer PSMs indicate an HTL-dependent degradation mechanism.

Fig. S8 shows the XRD results of the inactive area (regions on a module substrate not covered by the rear electrode) for uncycled and cycled PSMs. The δ-FAPbI$_3$ observed in the module area of cycled MeO-2PACz PSMs is not seen in the inactive area, indicating that the observed degradation is electrochemically driven by the device's built-in electric field. While the formation of a small AgI peak at $2\theta = 22.32°$ is noticeable in the module area for all HTL types, its relative intensity for cycled

samples is similar to that of uncycled samples, indicating MHP degradation that is independent of the stressing conditions. This demonstrates that a silver–halide reaction is not dominating the observed phase changes. Similarly, the inactive area of NiO$_x$ and bilayer PSMs contained no peak splitting or shifting associated with cation phase segregation, something which we will elaborate upon further when discussing additional stability tests.

Photoluminescence (PL) measurements were taken on postmortem cycled PSMs to compare relative intensities and peak positions, the results of which can be seen in Fig. 4(a). There is a clear shift in peak position in the module area as compared to the inactive area for NiO$_x$ and bilayer PSMs, while the nearly nonexistent peak under the module area of the MeO-2PACz PSM indicates the high presence of δ-FAPbI$_3$ and lack of a photoactive MHP phase. A visualization of this can be seen in Fig. 4(b)–(d) with maximum position maps generated from hyperspectral PL imaging. The PSMs in Fig. 4(a) are different from those in Fig. 4(b)–(d), however, they are representative of the trends observed. The images in Fig. 4(b)–(d) are taken at the border of the module and inactive areas, showing a noticeable
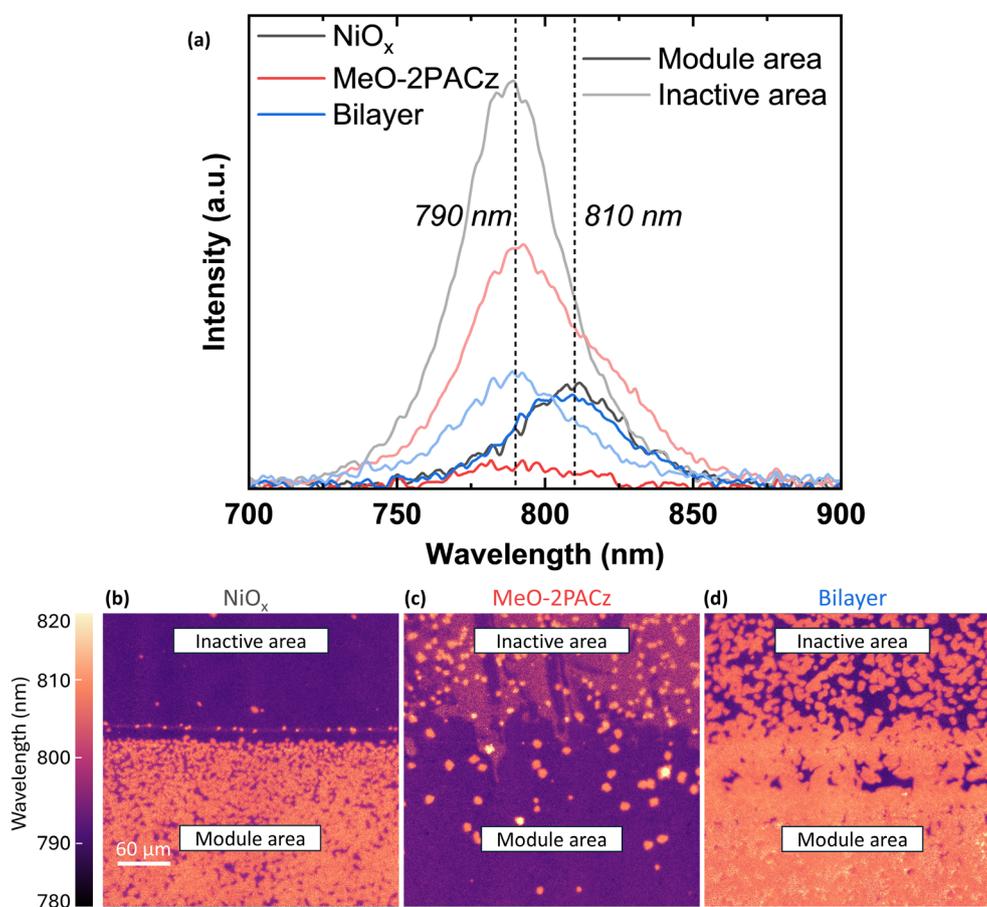

Fig. 4 (a) Photoluminescence (PL) results of post-mortem cycled PSMs comparing emission spectra of the MHP that was part of the module area to the inactive area (not covered by the rear electrode). Note the peak shifting present in the NiO$_x$ and bilayer module areas and the significantly reduced PL emission in the MeO-2PACz module area, due to cation phase segregation and the formation of δ-FAPbI$_3$, respectively. (b)–(d) Maximum position maps from hyperspectral PL images of NiO$_x$, MeO-2PACz, and bilayer PSMs, respectively, taken at the edge of the PSM. (b)–(d) utilize the same scale for PL emission and physical size.

peak shift for NiO$_x$ PSMs from ~790 nm (1.57 eV) under the inactive area to ~810 nm (1.53 eV) in the module area, in agreement with the cation phase segregation observed in XRD and steady-state PL measurements. The bilayer displays a more significant extent of the cation phase segregation immediately outside the module area, as Fig. 4(d) demonstrates regions bordering the module area as having a maximum intensity at ~810 nm. The presence of MeO-2PACz on NiO$_x$ may accelerate the cation phase segregation, as seen with the XRD and hyperspectral PL results; however, we will discuss the relevance of this finding in more detail later. Below we explore possible reasons for the HTL-dependent degradation.

Testing for moisture- and oxygen-induced degradation

Our initial hypothesis for the edge-initiated degradation seen with MeO-2PACz PSMs was that moisture and oxygen ingress was responsible for the observed phase changes. Previous work has shown that both moisture and oxygen are required for the rapid degradation of FA$_{1-x}$Cs$_x$PbI$_3$ MHPs into δ-FAPbI$_3$ and δ-CsPbI$_3$, and it was demonstrated that either stressor alone is not sufficient to induce rapid degradation of the MHP.[35] The UV resin encapsulant we utilized during thermal cycling has a relatively high water vapor transmission rate (WVTR) and was used without an additional material as the edge seal. Furthermore, our device architecture has a relatively short distance from the edge of the encapsulant to the edge of the module area (referred to as the edge seal width), on the order of 2–4 mm, leading to an architecture susceptible to moisture and oxygen ingress. In order to test the hypothesis that moisture/oxygen are the main stressors for the observed HTL-dependent degradation, we constructed test structures of a full device stack without electrical connections and adjusted two parameters: the encapsulant used and the edge seal width. We also constructed a test structure with no HTL (MHP in direct contact with ITO), as we hypothesized this would follow a similar degradation pathway as the MeO-2PACz sample. Table 1 lists the WVTRs of the two UV resins used for this experiment (Eversolar AB-302 and AB-341) as well as a third UV resin (AB-313) that was used to encapsulate half of the PSMs in Fig. 2(a). AB-302 and AB-313 were used interchangeably for PSM encapsulation during thermal cycling due to their nearly identical WVTRs. Polyisobutylene, the industry standard for moisture-barrier edge seals, is also listed in Table 1 for reference. We performed a separate study comparing all three UV resins listed in Table 1 for thermal cycling of encapsulated NiO$_x$ and MeO-2PACz PSCs, shown in Fig. S9. Overall, we did not observe any significant difference in the performance of the PSCs after 200 cycles,

regardless of the resin or HTL used, likely due to the larger edge seal width found on substrates containing PSCs instead of PSMs.

We adjusted the edge seal width of the test structures by performing an edge deletion of all device layers (carried out with laser ablation) to leave an 8 × 8 mm active area in the center of the substrate and by using two different sizes for the cover glass: a smaller cover glass similar to that used for PSM encapsulation (~10 × 10 mm), and a larger cover glass identical in size to the substrate (25 × 25 mm), leading to respective edge seal widths of ~2.5 and ~8.5 mm, as shown in Fig. 5(a). A cross-sectional schematic of the test structures is shown in Fig. 5(b). We subjected these test structures to the same thermal cycling conditions as the PSMs and photographed them. Fig. 5(c) shows photographs (from the ITO side) at 0 cycles, 200 cycles, and 7 days after 200 cycles (stored in dark/N$_2$) of the 4 architectures encapsulated with the higher WVTR resin (AB-302) and the smaller cover glass (2.5 mm edge seal width), the condition presumed to allow the greatest moisture/oxygen ingress and lead to the most significant degradation. Photographs of the remaining test structures are shown in Fig. S10 and S11. We observed that the only samples with visible degradation were the MeO-2PACz and ITO architectures with a 2.5 mm edge seal width and encapsulated with AB-302. Notably, while there was little discoloration seen in both the MeO-2PACz and ITO samples after 200 cycles, there was a significant amount of yellowing 7 days later after having been stored in the dark in an N$_2$ glovebox, similar to the degradation trend of cycled MeO-2PACz PSMs in Fig. 2. We did not observe any visible degradation of the MHP originating from cation phase segregation in any of the NiO$_x$ or bilayer structures that we had previously seen in PSMs after thermal cycling, reinforcing that illumination is necessary for cation phase segregation. It is worth noting that a systematic error in encapsulation of the 2.5 mm edge seal/AB-302 bilayer sample led to an even smaller edge seal width than 2.5 mm, yet no visible degradation was observed, as seen in Fig. 5(c).

Fig. 5(d) shows XRD scans of test structures encapsulated with AB-302 for both 2.5 and 8.5 mm edge seal widths. The XRD results of the remaining test structures encapsulated with AB-341 can be found in Fig. S12. The MeO-2PACz and bare ITO architectures with a 2.5 mm edge seal width encapsulated using AB-302 show a clear δ-FAPbI$_3$ and δ-CsPbI$_3$ presence—in fact, the ITO architecture completely converted into δ-FAPbI$_3$ and δ-CsPbI$_3$, as seen by the lack of the characteristic cubic MHP peaks. Fig. 5(e)–(g) shows magnified views of the XRD scans for the peaks corresponding to the (100), (200), and (210) planes, and it is evident that neither the NiO$_x$ nor bilayer structures display the peak shifting associated with cation phase segregation. These findings indicate a difference in the degradation mechanisms dependent on the HTL used: moisture/oxygen play a significant role in the degradation of MeO-2PACz PSMs, likely driven by contact of the MHP with the ITO, and moisture/oxygen and thermal cycling alone are not enough to drive the cation phase segregation seen in NiO$_x$ and bilayer PSMs. We would like to note that the MeO-2PACz and ITO samples without δ-FAPbI$_3$ formation (AB-302/8.5 mm and all AB-341

Table 1 Water vapor transmission rate (WVTR) of encapsulants

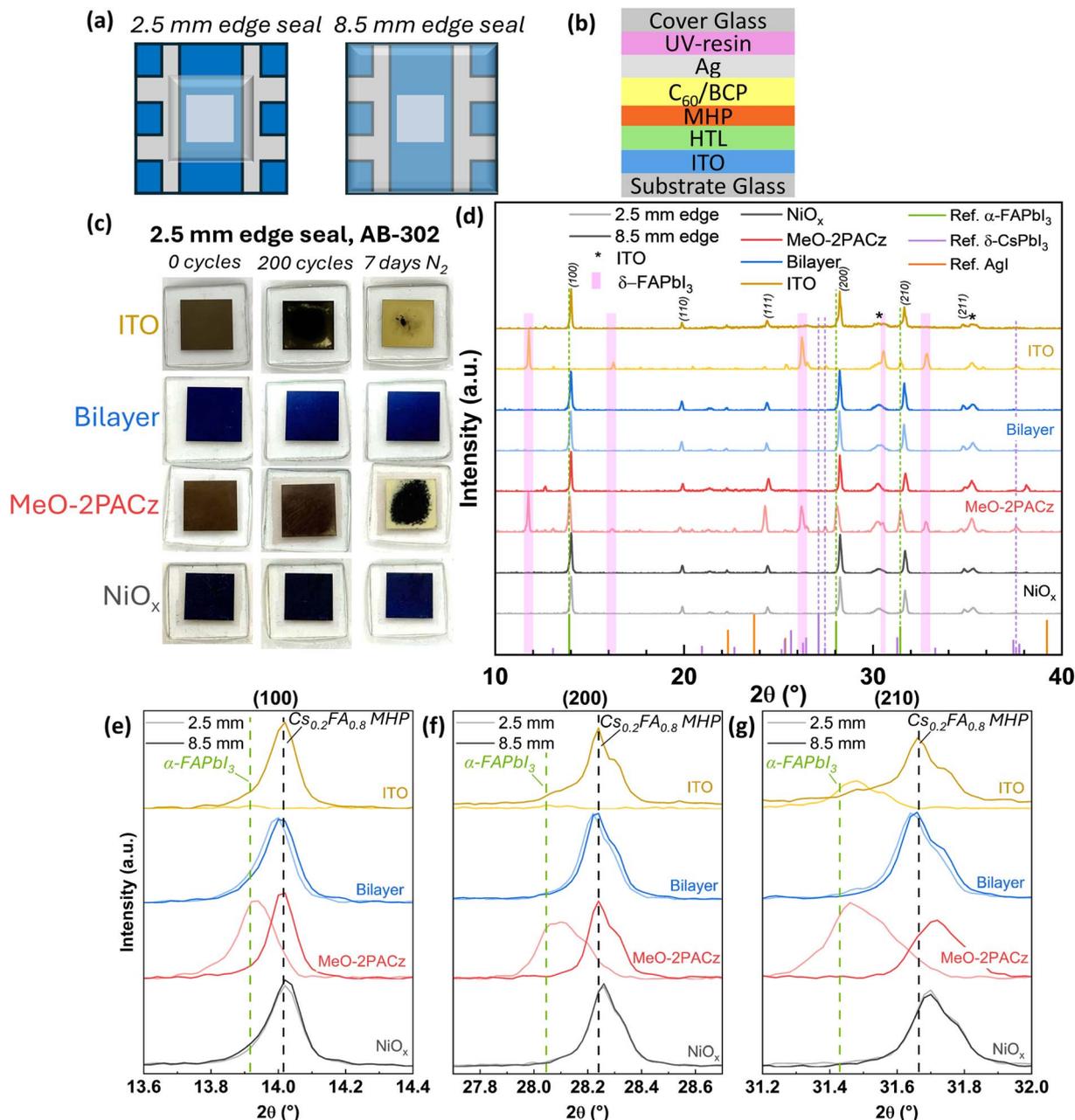| Encapsulant	WVTR (g m^{-2} days^{-1})
AB-302	< 4
AB-313	< 6
AB-341	< 10^{-2}
Polyisobutylene	~10^{-6}

Fig. 5 (a) Top-down view schematics of test structures with 2.5 mm and 8.5 mm edge seal widths. (b) Cross-sectional schematic of test structure architecture. (c) Photographs of test structures (from ITO side) to evaluate the effect of moisture/oxygen ingress for the three HTLs studied and a bare ITO architecture, using the UV resin AB-302 with a 2.5 mm edge-seal width. (d) XRD results of the test structures comparing differing edge seal widths (2.5 mm and 8.5 mm) of the four architectures encapsulated with the UV resin AB-302. The same reference patterns in Fig. 3d are shown here. (e) and (f) Magnified views of XRD results from (d) for the (100), (200), and (210) planes, respectively. Dashed vertical lines represent reference scans for α-FAPbI$_3$ (green) and a pristine double-cation MHP (black).

samples) displayed a noticeable PbI$_2$ peak ($2\theta = 12.67°$). Without moisture and oxygen ingress causing the formation of δ-FAPbI$_3$, a separate degradation mechanism occured involving the MHP and MeO-2PACz and/or MHP and ITO that formed PbI$_2$. This mechanism may be kinetically slower than the formation of δ-FAPbI$_3$ in the presence of moisture/oxygen, which would explain why we did not observe noticeable PbI$_2$ presence for samples containing δ-FAPbI$_3$. Below we propose

possible mechanisms for the observed HTL-dependent degradation.

Discussion of degradation mechanism observed in thermally cycled MeO-2PACz PSMs

Previous work has shown that high heat and reverse bias can accelerate etching of the ITO layer by A-site cation salts, leading to In^{3+} migration into the MHP layer and significant device

degradation.[36] Recent work expanded upon this and proposed that a positive feedback loop can be established wherein an initial stressor, such as moisture, can cause the formation of MHP degradation byproducts, such as HI, which in turn can etch the ITO layer to release In^{3+} and additional moisture, further degrading the MHP.[37] This proposed mechanism aligns well with our observations of MeO-2PACz and ITO structures: although there was minimal visible degradation in samples with moisture/oxygen ingress after 200 thermal cycles, storing the samples in N_2 for 7 days allowed any trapped moisture/oxygen to continue this positive feedback loop, rapidly destabilizing the perovskite lattice and forming large amounts of δ-$FAPbI_3$. While the previous result highlighted that an ETL such as SnO_x is porous enough to allow for the above mechanism to take place and utilized a chelating layer between the ITO and SnO_x to block HI passage, sol–gel NiO_x (annealed >300 °C) may be more dense than traditional nanoparticle SnO_x, allowing it to serve as a more effective barrier to prevent this mechanism.[38] The sensitivity of PSMs with thin, organic transport layers such as MeO-2PACz demonstrates the significance of how even marginal moisture/oxygen ingress can lead to rapid deterioration of PSMs without proper barrier layers between the MHP and ITO. A future study comparing different NiO_x deposition methods/thicknesses or alternative buffer layers that mitigate ion migration is therefore of value.[39]

An alternative mechanism we consider is more specific to the chemical composition of the MeO-2PACz molecule itself. Extensive work has shown that the phosphonic acid anchoring groups commonly found in carbazole-based SAMs (MeO-2PACz, 2PACz, Me-4PACz, *etc.*) can etch and corrode underlying metal oxide layers such as ITO and NiO_x, particularly as hydrolysis can decompose parts of the SAM molecule.[21] One study proposed the following mechanism involving the phosphonic acid group: hydrolysis of the P–O bond can produce a free hydroxyl group on the P atom, resulting in the formation of hydronium ions that are capable of etching the ITO and releasing In^{3+} and H_2O.[40] While the mechanism mentioned previously (MHP degrading from moisture/oxygen, leading to HI etching the ITO) explains the degradation seen in test structures with MHP on bare ITO, we cannot confirm the extent of the latter mechanism in this study.

In order to validate these mechanisms and explore the possibility of degradation of the ITO from acidic degradation byproducts, X-ray photoelectron spectroscopy (XPS) was carried out on the surface of cycled structures and compared against pristine ITO. Degradation of the ITO would result in a difference in the binding energy of the In 3d spectra as new chemical states are formed, with the most likely byproducts being $In(OH)_3$ and InI_3 as In^{3+} reacts with the MHP. Fig. 6 shows narrow scans of the In 3d spectra for two of the test structures in Fig. 5, labeled as follows: MHP/MeO-2PACz (thermally cycled without moisture ingress and no δ-$FAPbI_3$ formation) and δ-MHP/MeO-2PACz (thermally cycled with moisture ingress and δ-$FAPbI_3$ formation). A scan of pristine ITO is also shown for reference. The wide scans of each sample can be found in Fig. S13(a). It is worth noting that small scratches on the MHP surface due to handling allowed for probing of the ITO layer without completely removing the MHP. Although the
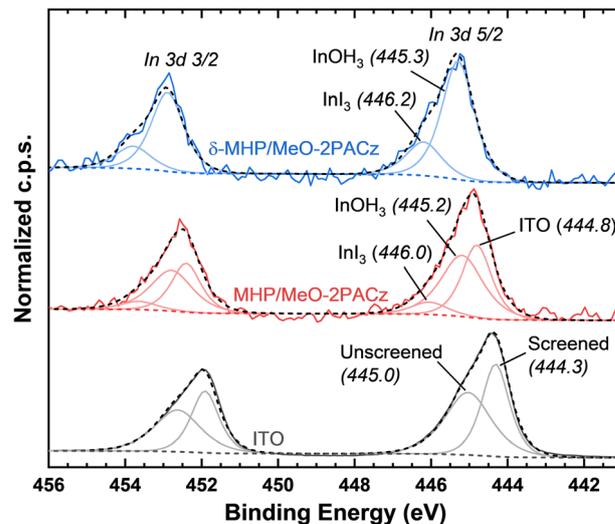

Fig. 6 XPS spectra of In 3d for ITO, MHP/MeO-2PACz (no δ-$FAPbI_3$), and δ-MHP/MeO-2PACz. Synthetic components are shown as light-colored lines and the total fitting is shown as a black dashed line. Backgrounds are shown as dashed colored lines.

presence of the MHP layer led to a reduced signal-to-noise ratio for the In 3d peak, complete removal of the MHP—either through physical scraping or dissolution of the MHP in DMF—was not performed. We speculate that complete MHP removal could remove the degradation byproducts formed between the In^{3+} and MHP.

Fitting of the In 3d 5/2 peak for pristine ITO can be carried out with two symmetrical components located at 444.3 and 444.9 eV; previous reports have shown that these two components do not represent different chemical states of In but are a result of screened and unscreened core holes, respectively, leading to two distinct energy states during photoemission.[41] The In 3d peaks for MHP/MeO-2PACz and δ-MHP/MeO-2PACz are shifted to progressively higher binding energies than that of the pristine ITO, indicative of different chemical states for In. Fitting of the MHP/MeO-2PACz spectra can be performed with three components representing the following compounds: ITO, $In(OH)_3$, and InI_3. Fitting of the ITO component for the MHP/MeO-2PACz spectra was performed with only one synthetic peak so as not to complicate the model, and its position aligns well with reported values. The δ-MHP/MeO-2PACz spectra displays an even higher energy shift and thus can only be fitted with two components with positions corresponding to $In(OH)_3$ and InI_3. The peak locations and FWHM for each component can be seen in Table S1 and agree reasonably well with the previous literature.[42–44] The significant shift of the In 3d peak for the δ-MHP/MeO-2PACz sample indicates a greater amount of $In(OH)_3$ and InI_3, likely resulting from more extensive degradation of the ITO, which can be correlated to increased δ-$FAPbI_3$ formation. Although we still observe degradation byproducts for the MHP/MeO-2PACz sample with no δ-$FAPbI_3$, we theorize this may be due to degradation of the ITO by the phosphonic acid group that has not yet triggered detrimental device performance and is independent of the positive feedback loop linked with δ-$FAPbI_3$ formation.

Fig. S13(b) shows the I 3d spectra of the aged samples compared to pristine MHP, showing a minimal shift. This is not entirely surprising because of the relatively small amount of InI_3 molecules compared to the host MHP-related iodine bonds and the very similar binding energies of iodine in the host MHP (619.3 eV) vs. InI_3 (619.1 eV). We believe that the formation of new In-containing compounds is compelling evidence that the positive feedback mechanism is occurring in samples with MeO-2PACz and moisture/oxygen ingress. We believe that the presence of NiO_x effectively prevents this mechanism from occurring.

Light-soaking to evaluate cation phase segregation in NiO_x/bilayer PSMs

In order to probe the phase segregation seen in cycled NiO_x and bilayer PSMs, we performed a study examining the effect of light-soaking on test structures identical to the four architectures explored in Fig. 5 (3 HTLs + MHP/ITO). We also illuminated a bilayer PSC substrate (containing 6 individual pixels). Cross-sectional schematics of the test structures and bilayer PSC can be seen in Fig. 7(a) and (b), respectively. Samples were encapsulated and illuminated in an N_2 glovebox for ~350 h (the bilayer PSC was illuminated for ~200 h) under 1-sun illumination. Photographs of the test structures and bilayer PSC (taken from the ITO side) can be seen in Fig. 7(c) and (d), respectively. Unlike the PSMs in Fig. 2, none of the full-coverage structures in Fig. 7(c) had any color change associated with cation phase segregation, while the bilayer PSCs in Fig. 7(d) had noticeable discoloration under the Ag pixels, similar to that seen in the module areas of cycled NiO_x/bilayer PSMs. XRD was performed on all samples after aging, the results of which are shown in Fig. 7(e). A magnified view of the peaks corresponding to the
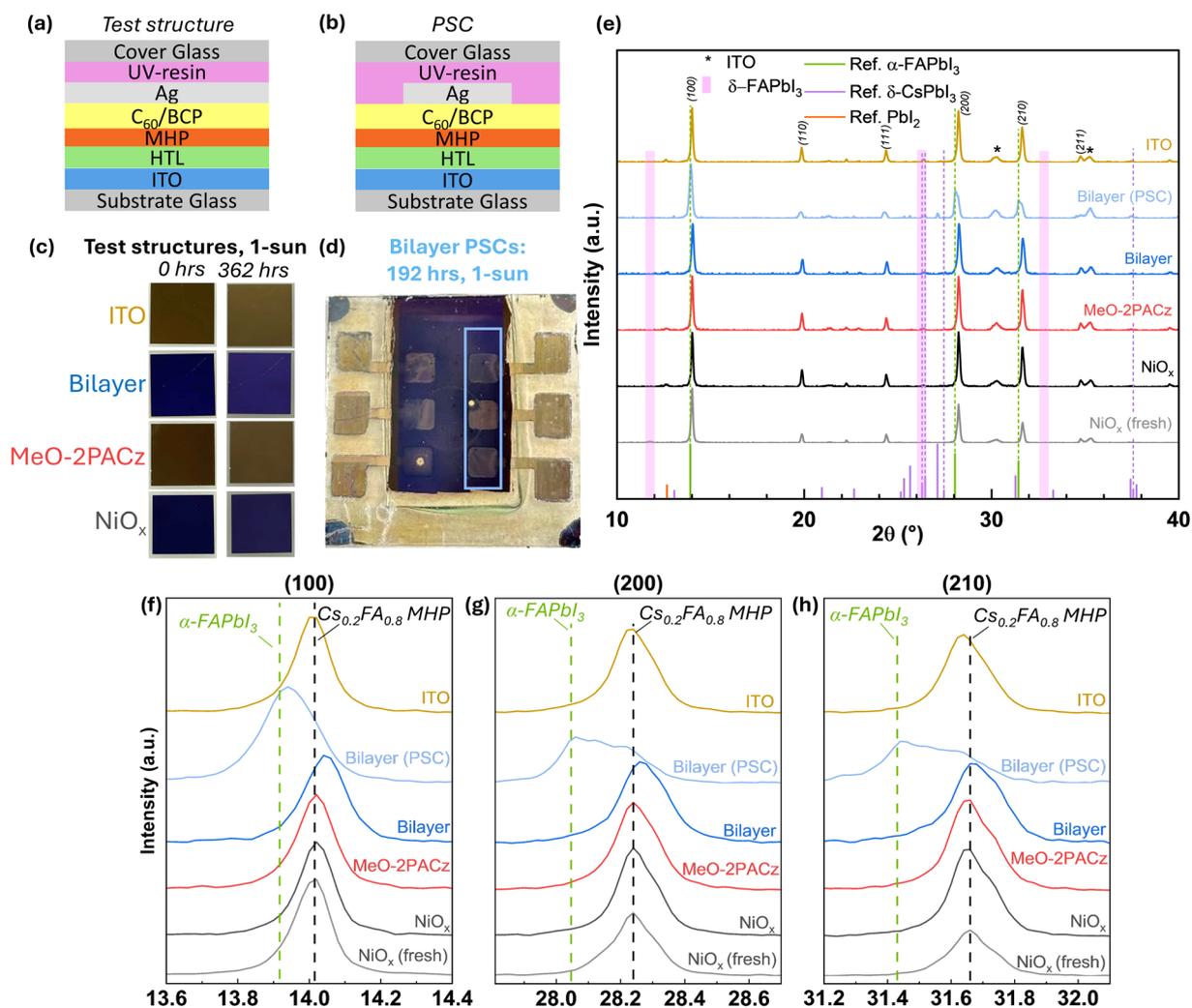

Fig. 7 (a) Cross-sectional view of test structures and (b) PSCs for illumination-based aging. (c) Photographs of encapsulated test structures (taken from ITO side) after illumination in N_2 for the three different HTLs and MHP directly on ITO. (d) Photograph of a bilayer PSC substrate (taken from ITO side) after ~200 h of illumination under the same conditions as those in (c). (e) XRD results for the samples shown in (c) and (d), along with a reference scan of freshly made MHP on NiO_x; the solid rectangle in (d) indicates the region explored with XRD for the bilayer PSC. (f)–(h) Magnified view of the XRD results from (e) of the (100), (200), and (210) planes, respectively, showing that peak shifting is present only in the bilayer PSCs sample after illumination.

(100), (200), and (210) planes is shown in Fig. 7(f)–(h). A reference XRD scan of a fresh NiO$_x$ PSM is shown in the XRD results for comparison. While the test structures with a full blanket coverage have no significant peak shifting/splitting after illumination, the bilayer PSCs display significant peak shifts to lower 2θ values, indicative of cation phase segregation. We would like to note that this did not appear to have a detrimental effect on the PCE of the bilayer PSCs as observed in Fig. S14, contrary to previous reports.[33] It may be that this extent of cation phase segregation is not as detrimental on small area devices. Below we explain a reason for the observed discrepancy with cation phase segregation.

Previous work has shown that the mechanism driving cation phase segregation under illumination arises from an energetic favorability to pass charge carriers through a pure α-FAPbI$_3$ phase, and a large amount of charge carriers generated upon illumination can overcome the entropy of mixing that formed the double-cation phase, thus leading to phase segregation.[33] Additionally, it has been shown that illuminating a substrate with an inactive area leads to a greater bias developing in the inactive area than in the device area, and this can lead to artificial degradation mechanisms not seen when using a photomask or module-relevant configuration (*i.e.*, full coverage).[45] We did not use a photomask during JV measurements of PSMs and PSCs, and the results from the test structures and bilayer PSCs in Fig. 7 indicate that the presence of the inactive area is playing a key role in the observed cation phase segregation. It is clear that module-relevant configurations (*i.e.*, samples with no inactive area) do not display cation phase segregation under these conditions. We therefore conclude that the key chemical degradation mechanism relevant to commercialized modules we have observed under these conditions is conversion of the MHP into δ-FAPbI$_3$ if in near/direct contact with the ITO layer in the presence of moisture/oxygen, and that the cation phase segregation we observed in cycled NiO$_x$/bilayer PSMs was an artificial degradation mechanism.

Conclusion

We highlight the differences in degradation in encapsulated p–i–n PSMs with three different HTL architectures: NiO$_x$, MeO-2PACz, and a bilayer consisting of MeO-2PACz deposited on NiO$_x$. NiO$_x$ and bilayer PSMs exhibit higher reproducibility and stability with thermal cycling than MeO-2PACz PSMs in the presence of moisture and oxygen ingress. Without a sufficiently thick, dense, and uniform HTL, contact between the MHP and ITO can lead to a positive feedback loop involving etching of the ITO from MHP degradation byproducts and further destabilization of the MHP, resulting in the formation of non-photoactive δ-FAPbI$_3$. Stressing under illumination revealed that cation phase segregation observed in cycled NiO$_x$/bilayer PSMs is an artificial degradation mechanism stemming from the presence of an inactive area that was not masked during JV-testing. We highlight the importance of testing multiple stressors at once to determine field-relevant degradation mechanisms of PSMs and the necessity to consider the buried charge transport layer selection for the commercial

advancement of PSMs. We lastly emphasize that there are thermomechanical degradation modes at the panel scale ($\sim$m^2) which were not tested in this study that warrant further investigation and consideration.

Experimental section

Materials

NiO$_x$ ink was prepared using nickel(II) nitrate hexahydrate (Sigma-Aldrich-99.99%), anhydrous ethylene glycol (EG) (Thermo Fischer Scientific-99.8%), and ethylene diamine (EDA) (Thermo Fischer Scientific-99%).

MeO-2PACz ink was prepared using [2-(3,6-dimethoxy-9*H*-carbazol-9-yl)ethyl] phosphonic acid (MeO-2PACz) (TCI America-98% purity) and anhydrous ethanol (Thermo Fischer Scientific-99.5+%).

MHP ink was prepared using cesium iodide (CsI) (Sigma-Aldrich-99.999% trace metal basis), formamidinium iodide (FAI) (Great Cell Solar Materials-99.99%), lead-iodide PbI$_2$ (TCI America-99.99%), *N,N*-dimethyl formamide (DMF) (Sigma-Aldrich-99.8%), and 1-methyl-2-pyrrolidinone (NMP) (Thermo Fischer Scientific-99+%, ACS reagent).

Fullerene (C$_{60}$) (TCI-99.5%, purified by sublimation), bath-ocuproine (BCP) (TCI-99%, purified by sublimation) and Ag pellets (TCI-99%) were thermally evaporated as the electron transport layer, buffer layer, and rear electrode, respectively. All materials were used as received without further purification.

Cell and module fabrication

Substrate preparation. Indium-tin oxide (ITO) patterned 25 × 25 mm glass substrates were purchased from Xin Yan Technical group ($R_{\text{sheet}} = 10 \ \Omega/$). Substrates were cleaned before film deposition in the following manner: scrubbed with a brush with a solution of 1 : 10 extran : water, rinsed thoroughly under DI water, and sonicated for 15 minutes in DI water, acetone, and IPA. Substrates were dried with an N$_2$ gun in between each sonication step. Substrates were then surface treated using UV-ozone for 15 minutes immediately before HTL deposition.

HTL deposition. For NiO$_x$-based PSCs and PSMs, nickel(II) nitrate hexahydrate was dissolved in a 96 : 4 volume ratio of ethylene glycol and ethylene diamine to make 1 M NiO$_x$ sol–gel. The ethylene diamine was added to the solution after the ethylene glycol. Prior to deposition, NiO$_x$ sol–gel was filtered using a 0.22 μm PVDF filter. NiO$_x$ sol–gel was spin coated in ambient conditions on cleaned substrates by dispensing $\sim$80 μL of 1 M NiO$_x$ sol–gel and spinning at 5000 rpm for 30 seconds with an acceleration of 2500 rpm s^{-1}, and samples were subsequently annealed at $\sim$320 °C for 60 minutes in ambient conditions. For MeO-2PACz-based PSCs and PSMs, 1.5 mg mL^{-1} of [2-(3,6-dimethoxy-9*H*-carbazol-9-yl)ethyl] phosphonic acid powder was dissolved in ethanol in an N$_2$ glovebox and shaken at 600 rpm for 10 minutes and sonicated for at least 15 minutes before spin coating. MeO-2PACz solution was spin coated on freshly cleaned ITO substrates at 3000 rpm for 30 seconds with an acceleration of 1000 rpm s^{-1} followed by annealing at 100 °C for 5 minutes. Prior to beginning spinning, MeO-2PACz

solution was allowed to rest on the ITO substrate for ~20 seconds to allow the phosphonic acid groups to self-assemble. The MeO-2PACz layer in bilayer PSCs and PSMs was deposited directly on NiO_x without any treatment of the NiO_x and using the same deposition parameters for MeO-2PACz devices. Deposition of the MeO-2PACz layer in bilayer PSCs and PSMs was carried out within 1 hour of finishing the NiO_x annealing step.

MHP deposition. 1.4 M $Cs_{0.2}FA_{0.8}PbI_3$ MHP solution was prepared in an N_2 glovebox in a 1:6.5 volume ratio of NMP:DMF and shaken for at least 90 minutes at 700 rpm. The MHP solution was filtered using a 0.22 μm PVDF filter prior to deposition. MHP films were deposited through a 2-step gas-quench assisted spin coating method in the following manner: 500 rpm for 10 seconds with 250 rpm s^{-1} acceleration followed by a second spin step of 5000 rpm for 34 seconds with an acceleration of 1125 rpm s^{-1}. 100 μL of MHP solution was used for deposition on NiO_x, while 150–200 μL of MHP solution was necessary for complete coverage of MeO-2PACz or bilayer devices. 10 seconds after reaching the desired final spin speed in the second step (i.e., 14 seconds into the second spin step to account for 4 seconds of ramp-up time), the N_2 flow was opened using a manual regulator inside the glovebox to quench the film for the remaining 20 seconds of spinning. NiO_x, MeO-2PACz, and bilayer devices were quenched with N_2 flowrates of 3.8, 4.3, and 4.9 standard cubic feet per minute (scfm), respectively, as each HTL was found to have differing optimal gas quench flowrates. Optimization of gas quench flowrates for the MHP on each HTL can be seen in Fig. S15 as PSC performances are compared. Bilayer PSCs displayed little variation with quenching flowrates, so 4.3 scfm was used as it displayed the tightest data distribution. The gas quench outlet was positioned ~2.5 cm above the substrate. The gas quench setup was arranged in the following manner:[46] in house N_2 was supplied through a rigid Nylon tube (McMaster Item#: 5548K74) with an outer diameter (OD) of 1/4″ and inner diameter (ID) of 11/64″ and delivered to a 6″ long metal pipe (Grainger Item#: 1XBT4) with an OD of 11/16″ and ID of 1/2″. A manual regulator and flowmeter (McMaster Item#: 8051K218) were placed in the gas quench setup between the N_2 supply and gas quench straw in order to report standardized quenching conditions. The N_2 glovebox was kept purging during MHP deposition.

ETL, buffer layer, and rear electrode deposition. For electron transport and buffer layer deposition, C_{60} and BCP were thermally evaporated using an Angstrom evaporator inside an N_2 glovebox at a rate of 0.2 Å s^{-1} to yield 25 nm and 4 nm thick films, respectively. Ag evaporation was carried out in the same evaporator at a rate of 1 Å s^{-1} for a rear electrode thickness of 100 nm. Edge deletion with a razor blade was carried out prior to Ag evaporation to reduce degradation of the contact pads at the Ag/MHP interface. A shadow mask was used to create individual pixels (i.e., PSCs) for a total of 6 pixels per substrate (for PSCs) or two PSMs per substrate (for PSMs), with contact pads extending beyond the active area.

Laser scribing for PSM fabrication. PSMs were fabricated in a similar manner as described for PSCs with the addition of laser scribing to introduce monolithic series interconnection

between cells. P1, P2, and P3 laser scribing was all performed using a Keyence UV-ns laser (MD-U1000C). Parameters for each scribe (differing also by HTL for the P2 scribe) can be seen in Table S2. Fluence calculations of each laser pulse were calculated with the knowledge of the laser marking energy (displayed by the laser marking software), a laser spot size of 25 μm (with the laser spot focused on the substrate), and relevant marking conditions (scan speed, frequency, and repetitions). The P1 scribe, necessary for electrical isolation of the front ITO contact, was performed prior to substrate cleaning. The P2 scribe was performed after deposition of the final active layer (BCP) and before the rear electrode (Ag) to allow for interconnection of cells, and the P3 scribe was performed after Ag deposition to electrically isolate cells on the rear electrode. The P2 and P3 scribes utilized a rastering technique in which subsequent repetitions of the scribe are shifted by a set distance (3 μm for all scribes using rastering) to avoid damaging underlying layers with excessive ablation. To avoid any sort of electrical connectivity between the 2 PSMs on a substrate, a pseudo-P4 scribe (utilizing P1 scribe conditions) was placed horizontally in the center of the substrate between the two PSMs in order to ablate through all active layers and the ITO. A diagram of the module substrate can be seen in Fig. 1(b).

Encapsulation of PSCs and PSMs. Encapsulation was carried out with a UV-curable resin acquired from Everlight Chemical USA (WVTR values for the resins were provided by Everlight Chemical as well). Three different UV resins were used throughout this study: Eversolar AB-302, AB-313, and AB-341. Microscope slides (Globe Scientific Item#: 1321) were cut down to an appropriate size to be used as a cover glass for encapsulation and were scrubbed with a solution of 1:10 extran:water, rinsed thoroughly in DI water, dried with an N_2 gun, and baked at 150 °C for at least 10 minutes prior to encapsulation, which was performed in ambient conditions. In order to encapsulate devices, a small amount of UV resin was dropped onto the cover glass which was then pressed on the sample substrate to cover the cell/module area and held in place for ~1 minute with a 2 kg weight. Once the weight was removed and after ensuring no air bubbles were visible in the UV resin, samples were brought under a UV lamp (365 nm, 300 W) for ~30 seconds to allow the resin to cure. For the test structures exploring the effect of moisture/oxygen and light, the encapsulation technique was the same as described above with the addition of significant edge deletion prior to encapsulation, first with a razor blade and then with P3-equivalent laser ablation, leaving an active area of 8 × 8 mm in the center of the 25 × 25 mm ITO-patterned glass substrate.

Slight changes in PSM and PSC performance with encapsulation over time were observed. Fig. S2 shows cell performance before, immediately after, and 3 days after encapsulation (referred to as "Fresh", "Encap Immediate" and "3 days N_2") compared to unencapsulated PSCs. Values have been normalized to the mean of "Fresh" PSCs for each sample type, and unencapsulated PSCs utilized the same measurements for "Encap Immediate" as they did for "Fresh". We attribute the improvement of encapsulated PSCs to the nature of the encapsulation process: pressing down on the device stack with

a 2 kg weight may improve the interfacial contact between layers and thus reduce series resistance and heal shunts.[47] Devices had the largest change in PCE 3–5 days after encapsulation, so we collected the 0-cycle measurements 6 days after encapsulation and storage in an N_2 glovebox before beginning thermal cycling for PSMs.

Thermal cycling procedure

Thermal cycling was carried out in an environmental chamber (Thermotron Item#: SM-8-8200) following adapted guidelines of IEC 61215: starting at room temperature, samples were cycled from −40 to 85 °C at an accelerated rate of 4 °C min^{-1} with a dwell time of 10 minutes. The relative humidity (RH) was set to 25%, however each cycle presented spikes above 70% RH when the chamber temperature dropped below 10 °C. Devices were measured and photographed every 100 cycles.

Light-soaking

Light-soaking of PSCs was performed in an N_2 glovebox under 1-sun illumination using a Newport Class ABA LED Solar Simulator (MiniSol™: LSH-7320) that was calibrated using an Asahi Spectra 1-sun checker. JV-sweeps of bilayer PSCs were performed every 24 hours until 96 h, and then after 192 total h. Light-soaking of the PSCs began 20 days after initial encapsulation of PSCs (stored in the dark in N_2), and the 0 h measurement was performed immediately before light-soaking. Illumination-test structures were photographed every 24 hours until 362 hours, after which they were delaminated for XRD analysis.

Characterization

Bragg–Brentano X-ray diffraction (XRD) was carried out using a Rigaku high-resolution X-ray diffractometer from $2\theta = 5$–$50°$ with a step size of 0.02° and a scan speed of 2.5° min^{-1}. A 2 mm soller slit was used and the incident slit was 0.5°. A β-blocking Ni-foil was used before the receiving slit. A 2 mm length-limiting slit was used to ensure accurate sampling of specified areas (the width of the PSM area is 2 mm).

Photoluminescence (PL) measurements were carried out using a BLACK-Comet UV-vis Spectrometer from StellarNet with a laser excitation wavelength of 425 nm and integration time of 400 ms. The laser spot size (∼1 mm) was small enough to accurately probe differences in PL signal between the module and inactive areas of PSM substrates.

Current–voltage scans to measure PSC and PSM performance were measured using an Asahi Spectra HAL-320 Xenon solar simulator as a light source, calibrated with an Asahi Spectra 1-sun checker. Voltage sweeps were carried out with a Keithley 2450 in the reverse direction from 1.2 V to −0.2 V for PSCs and 2.4 V to −0.2 V for PSMs with a voltage step size of 0.014 V and dwell time of 10 ms.

Hyperspectral photoluminescence imaging was carried out using a Photon *etc.* IMA hyperspectral microscope as samples were illuminated by a 405 nm laser. Hyperspectral PL cubes were gathered at a 10-sun equivalent intensity calculated using

an ideal J_{sc} of 26.5 mA cm^{-2} for the chosen MHP ($E_g = 1.57$ eV) using the following equation:

$$P_{1\text{ sun}} = \frac{J_{sc,ideal} \times hc}{\lambda}$$

where $P_{1\text{ sun}}$ is the necessary laser irradiance for a photon flux equivalent to 1-sun, hc is a physical constant equal to 1240 eV nm, and λ is the incident laser wavelength (405 nm).[48] As such, the necessary laser irradiance equivalent to 1-sun of photon flux $P_{1\text{ sun}} = 81$ mW cm^{-2}, and the corresponding equivalent to 10-suns of photon flux $P_{10\text{ suns}} = 810$ mW cm^{-2}. The laser spot size is equivalent to the aperture of the 20× objective used for imaging ($A = 6.36 \times 10^{-3}$ cm^2), leading to a necessary laser output power $P_{out} = 5.16$ mW for a 10-sun equivalent photon flux. Due to losses of laser power prior to illumination of the sample, calibration of the laser input power was necessary to achieve the desired irradiance and was performed with a Thorlabs PM121D laser meter. This resulted in a laser input power of 54 mW to achieve a power of 5.16 mW at the sample surface. Imaging was performed with fully open apertures, and emission scans were collected from 700–900 nm with a step size of 2 nm. Dark images for references scans were taken for each sample to standardize intensities. Maximum position maps (MPM) were generated using the PhySpec software once cubes were calibrated to their dark reference.

X-ray photoelectron spectroscopy was carried out using a Kratos Axis Supra$^+$ X-ray photoelectron spectrometer with a monochromatic Al X-ray source (1487 eV) with an emission current of 5.00 mA and voltage of 15 kV. A step size of 1.0 eV was used for all scans, and a pass energy of 80 and 20 eV was used for wide and narrow scans, respectively. A charge neutralizer was used on all samples with an accelerating voltage of 1 eV. The analyzer was operated in fixed analyzer transmission mode. All samples were charge-corrected using the main signal of the carbon 1s spectrum assigned to 284.8 eV. The C (1s) spectra was collected using high energy resolution settings.

Author contributions

Conceptualization: M. C. and N. R.; methodology: M. C. and N. R.; investigation: M. C., S. P.; validation: M. C.; formal analysis: M. C.; data curation: M. C.; visualization: M. C. and N. R.; writing – original draft: M. C. and N. R.; writing – review and editing: M. C., S. P., W. N., N. R.; project administration: W. N. and N. R.; funding acquisition: W. N. and N. R. All authors discussed the results and commented on the manuscript.

Conflicts of interest

The authors declare no conflicts of interest.

Data availability

The data that support the findings of this study are available from the corresponding author upon reasonable request.

Supplementary information is available. See DOI: **https://doi.org/10.1039/d5el00083a**.

References

1 Best Research-Cell Efficiency Chart, National Renewable Energy Laboratory, accessed: Sep. 24, 2023, https://www.nrel.gov/pv/cell-efficiency.html.

2 C. C. Boyd, R. Cheacharoen, T. Leijtens and M. D. McGehee, Understanding Degradation Mechanisms and Improving Stability of Perovskite Photovoltaics, *Chem. Rev.*, 2019, **119**(5), 3418–3451, DOI: 10.1021/acs.chemrev.8b00336.

3 H. Jiao, *et al.*, Metal Halide Perovskite Solar Module Encapsulation Using Polyolefin Elastomers: The Role of Morphology in Preventing Delamination, *PRX Energy*, 2024, **3**(2), 2768–5608, DOI: 10.1103/prxenergy.3.023013.

4 S. Svanström, T. J. Jacobsson, G. Boschloo, E. M. J. Johansson, H. Rensmo and U. B. Cappel, Degradation Mechanism of Silver Metal Deposited on Lead Halide Perovskites, *ACS Appl. Mater. Interfaces*, 2020, **12**(6), 7212–7221, DOI: 10.1021/acsami.9b20315.

5 M. T. Mbumba, D. M. Malouangou, J. M. Tsiba, L. Bai, Y. Yang and M. Guli, Degradation mechanism and addressing techniques of thermal instability in halide perovskite solar cells, *Sol. Energy*, 2021, **230**, 954–978, DOI: 10.1016/j.solener.2021.10.070.

6 S. Uličná, *et al.*, Field-Relevant Degradation Mechanisms in Metal Halide Perovskite Modules, *Adv. Energy Mater.*, 2025, **15**(23), DOI: 10.1002/aenm.202404518.

7 F. Jamaatisomarin, R. Chen, S. Hosseini-Zavareh and S. Lei, Laser Scribing of Photovoltaic Solar Thin Films: A Review, *J. Mater. Process. Manuf. Sci.*, 2023, **7**(3), 94, DOI: 10.3390/jmmp7030094.

8 N. Phung, *et al.*, Enhanced Self-Assembled Monolayer Surface Coverage by ALD NiO in p-i-n Perovskite Solar Cells, *ACS Appl. Mater. Interfaces*, 2022, **14**(1), 2166–2176, DOI: 10.1021/acsami.1c15860.

9 J. Suo, B. Yang, D. Bogachuk, G. Boschloo, and A. Hagfeldt, *The Dual Use of SAM Molecules for Efficient and Stable Perovskite Solar Cells*, John Wiley and Sons Inc, 2024, DOI: 10.1002/aenm.202400205.

10 A. R. M. Alghamdi, M. Yanagida, Y. Shirai, G. G. Andersson and K. Miyano, Surface Passivation of Sputtered NiOx Using a SAM Interface Layer to Enhance the Performance of Perovskite Solar Cells, *ACS Omega*, 2022, **7**(14), 12147–12157, DOI: 10.1021/acsomega.2c00509.

11 W. Li, E. Martínez-Ferrero and E. Palomares, *Self-assembled Molecules as Selective Contacts for Efficient and Stable Perovskite Solar Cells*, Royal Society of Chemistry, 2023, DOI: 10.1039/d3qm01017a.

12 Z. Li, *et al.*, Stabilized hole-selective layer for high-performance inverted p-i-n perovskite solar cells, *Science*, 2023, **382**(6668), 284–289, DOI: 10.1126/science.ade9637.

13 T. Wu *et al.*, *Self-Assembled Monolayer Hole-Selective Contact for Up-Scalable and Cost-Effective Inverted Perovskite Solar Cells*, John Wiley and Sons Inc, 2024, DOI: 10.1002/adfm.202316500.

14 F. Jiang, *et al.*, Improved reverse bias stability in p–i–n perovskite solar cells with optimized hole transport materials and less reactive electrodes, *Nat. Energy*, 2024, 1275–1284, DOI: 10.1038/s41560-024-01600-z.

15 C. C. Boyd, *et al.*, Overcoming Redox Reactions at Perovskite-Nickel Oxide Interfaces to Boost Voltages in Perovskite Solar Cells, *Joule*, 2020, **4**(8), 1759–1775, DOI: 10.1016/j.joule.2020.06.004.

16 A. Magomedov, *et al.*, Self-Assembled Hole Transporting Monolayer for Highly Efficient Perovskite Solar Cells, *Adv. Energy Mater.*, 2018, **8**(32), DOI: 10.1002/aenm.201801892.

17 C. Liu, *et al.*, Efficient All-Perovskite Tandem Solar Cells with Low-Optical-Loss Carbazolyl Interconnecting Layers, *Angew. Chem., Int. Ed.*, 2023, **62**(51), DOI: 10.1002/anie.202313374.

18 C. Shi, *et al.*, Modulating competitive adsorption of hybrid self-assembled molecules for efficient wide-bandgap perovskite solar cells and tandems, *Nat. Commun.*, 2025, **16**, DOI: 10.1038/s41467-025-58111-y.

19 X. Zheng, *et al.*, Co-deposition of hole-selective contact and absorber for improving the processability of perovskite solar cells, *Nat. Energy*, 2023, **8**(5), 462–472, DOI: 10.1038/s41560-023-01227-6.

20 Q. Jiang, *et al.*, Towards linking lab and field lifetimes of perovskite solar cells, *Nature*, 2023, **623**(7986), 313–318, DOI: 10.1038/s41586-023-06610-7.

21 J. Wang, *et al.*, Less-acidic boric acid-functionalized self-assembled monolayer for mitigating NiOx corrosion for efficient all-perovskite tandem solar cells, *Nat. Commun.*, 2025, **16**(1), 4148, DOI: 10.1038/s41467-025-59515-6.

22 D. Wang, *et al.*, Rigid molecules anchoring on NiOx enable >26% efficiency perovskite solar cells, *Joule*, 2025, **9**(3), 101815, DOI: 10.1016/j.joule.2024.101815.

23 M. Dussouillez, *et al.*, Understanding and Mitigating the Degradation of Perovskite Solar Cells Based on a Nickel Oxide Hole Transport Material during Damp Heat Testing, *ACS Appl. Mater. Interfaces*, 2023, **15**(23), 27941–27951, DOI: 10.1021/acsami.3c02709.

24 L. Li, *et al.*, Flexible all-perovskite tandem solar cells approaching 25% efficiency with molecule-bridged hole-selective contact, *Nat. Energy*, 2022, 7(8), 708–717, DOI: 10.1038/s41560-022-01045-2.

25 X. Zhu, *et al.*, Inverted planar heterojunction perovskite solar cells with high ultraviolet stability, *Nano Energy*, 2022, **103**, 107849, DOI: 10.1016/j.nanoen.2022.107849.

26 J. Sun, *et al.*, NiOx-Seeded Self-Assembled Monolayers as Highly Hole-Selective Passivating Contacts for Efficient

Inverted Perovskite Solar Cells, *Sol. RRL*, 2021, **5**(11), DOI: **10.1002/solr.202100663**.

27 P. Holzhey and M. Saliba, A full overview of international standards assessing the long-term stability of perovskite solar cells, *J. Mater. Chem. A*, 2018, **6**, 21794–21808, DOI: **10.1039/C8TA06950F**.

28 J. A. Steele, *et al.*, Direct Laser Writing of δ- To α-Phase Transformation in Formamidinium Lead Iodide, *ACS Nano*, 2017, **11**(8), 8072–8083, DOI: **10.1021/acsnano.7b02777**.

29 C. Yang, *et al.*, Anisotropic δ-to-α Phase Transition in Formamidinium Lead Iodide Thin Films, *ACS Nano*, 2025, 9225–9231, DOI: **10.1021/acsnano.5c00037**.

30 D. Fabini, *et al.*, Reentrant structural and optical properties and large positive thermal expansion in perovskite formamidinium lead iodide, *Angew. Chem., Int. Ed.*, 2016, **55**(49), 15392–15396, DOI: **10.1002/anie.201609538**.

31 D. M. Trots, *et al.*, High-temperature structural evolution of caesium and rubidium triiodoplumbates, *J. Phys. Chem. Solids*, 2008, **69**(10), 2520–2526, DOI: **10.1016/j.jpcs.2008.05.007**.

32 *Natl. Bur. Stand. Circ. (U. S.)*, 1959, **539**, 51.

33 N. Li, *et al.*, Microscopic Degradation in Formamidinium-Cesium Lead Iodide Perovskite Solar Cells under Operational Stressors, *Joule*, 2020, **4**(8), 1743–1758, DOI: **10.1016/j.joule.2020.06.005**.

34 Z. Huang, *et al.*, Local A-Site Phase Segregation Leads to Cs-Rich Regions Showing Accelerated Photodegradation in Mixed-Cation Perovskite Semiconductor Films, *ACS Energy Lett.*, 2024, **9**(6), 3066–3073, DOI: **10.1021/acsenergylett.4c00960**.

35 J. Hidalgo, *et al.*, Synergistic Role of Water and Oxygen Leads to Degradation in Formamidinium-Based Halide Perovskites, *J. Am. Chem. Soc.*, 2023, **145**(45), DOI: **10.1021/jacs.3c05657**.

36 R. A. Kerner and B. P. Rand, Electrochemical and Thermal Etching of Indium Tin Oxide by Solid-State Hybrid Organic-Inorganic Perovskites, *ACS Appl. Energy Mater.*, 2019, **2**(8), 6097–6101, DOI: **10.1021/acsaem.9b01356**.

37 C. Zhan, C. Luo, F. Gao, X. Wang, Y. Li and Q. Zhao, Indium Tin Oxide Induced Internal Positive Feedback and Indium Ion Transport in Perovskite Solar Cells, *Angew. Chem., Int. Ed.*, 2024, **63**(30), DOI: **10.1002/anie.202403824**.

38 T. Ivanova, A. Harizanova, M. Shipochka and P. Vitanov, Nickel Oxide Films Deposited by Sol-Gel Method: Effect of Annealing Temperature on Structural, Optical, and Electrical Properties, *Materials*, 2022, **15**(5), 1742, DOI: **10.3390/ma15051742**.

39 Q. Wang, *et al.*, Cross-layer all-interface defect passivation with pre-buried additive toward efficient all-inorganic perovskite solar cells, *Carbon Energy*, 2024, **6**(9), DOI: **10.1002/cey2.566**.

40 F. A. Angel, Y. L. Lyubarskaya, A. A. Shestopalov and C. W. Tang, Degradation of self-assembled monolayers in organic photovoltaic devices, *Org. Electron.*, 2014, **15**(12), 3624–3631, DOI: **10.1016/j.orgel.2014.10.004**.

41 C. Körber, *et al.*, Electronic structure of In2 O3 and Sn-doped In 2 O3 by hard x-ray photoemission spectroscopy, *Phys. Rev. B:Condens. Matter Mater. Phys.*, 2010, **81**, 165207, DOI: **10.1103/PhysRevB.81.165207**.

42 J. F. Moulder and J. Chastain, *Handbook of X-Ray Photoelectron Spectroscopy : a Reference Book of Standard Spectra for Identification and Interpretation of XPS Data*. Physical Electronics Division, Perkin-Elmer Corp., 1992.

43 J. D. Henderson, L. Pearson, H. Y. Nie and M. C. Biesinger, X-Ray Photoelectron Spectroscopy Analysis of Indium and Indium-Containing Compounds, *Surf. Interface Anal.*, 2025, **57**(1), 81–97, DOI: **10.1002/sia.7356**.

44 G. E. McGuire, G. K. Schweitzer and A. Thomas Carlson, Study of Core Electron Binding Energies in Some Group IIIa, Vb, and VIb Compounds, *Inorg. Chem.*, 1973, **12**(10), 2450–2453.

45 R. Tirawat, *et al.*, Measuring metal halide perovskite single cell degradation consistent with module-based conditions, *Sustain. Energy Fuels*, 2024, **8**(3), 546–553, DOI: **10.1039/d3se01268a**.

46 S. C. Kaczaral, *et al.*, Improved reproducibility of metal halide perovskite solar cells *via* automated gas quenching, *Appl. Energy*, 2023, **1**(3), DOI: **10.1063/5.0174396**.

47 E. Burgard, S. Penukula, M. Casareto and N. Rolston, Pressure Engineering to Enable Improved Stability and Performance of Metal Halide Perovskite Photovoltaics, *Molecules*, 2025, **30**(6), DOI: **10.3390/molecules30061292**.

48 Z. Leuty, Scaling Emerging Solar Cell Technologies: Innovative Methods Materials, and Metrology, Doctorate thesis, Arizona State University, 2024, pp. 47–59.